Journal of Engineering Mechanics and Machinery (2024)
Clausius Scientific Press, Canada

DOI: 10.23977/jemm.2024.090115
ISSN 2371-9133 Vol. 9 Num. 1

Study on a Helix-Loaded Azimuthally Periodic Circular Waveguide for Short-Millimeter Wave TWT

Yang Liu, Xuying Zhang, Jun Wang, Yujiang Zhao, Bing Feng

Science and Technology on Electronic Information Control Laboratory, Chengdu, 610000, China

Keywords: Transmitter, traveling wave tube, slow wave structure, novel helix, azimuthally periodic waveguide, dispersion characteristics, interaction impedance, spatial harmonics method

Abstract: The transmitter is a key component in electronic systems and equipment for amplifying signal power, and the traveling wave tube (TWT) is a core component that realizes the key performance within the transmitter. For a long time, the slow wave structure (SWS) has been a key factor that restricts the improvement of TWT performance and the reduction of costs, which in turn limits the overall output power and operating frequency band of the transmitter. Therefore, the potential of helix slow wave structure(SWS) working at W band and higher frequency range is considered and the novel helix SWS is presented for high power wideband TWT in this paper. The proposed novel SWS consists of helixes that are arranged periodically about the axis of the conventional dielectric-lined circular waveguide. Here, the helixes are fixed in the dielectric layer, and a solid electron beam with larger radius passes through the waveguide center. The slow-wave dispersion equation and interaction impedance expression are obtained by the spatial harmonics method. The effects of the SWS parameters on the RF characteristics, including the pitch and the thickness and the angle of the helixes, are numerically calculated and discussed. It is indicated that selecting the appropriate thickness and angle of the helixes can increase the interaction impedance with only slight influence on the dispersion characteristics (pitch fixed). Moreover, compared with a dielectric-lined azimuthally periodic circular waveguide (DLAP-CW), the novel circuit is much shorter than the DLAP-CW-based circuit with good performance at the working frequencies. The HLAP-CW, therefore, will favor the miniaturized design of a high-power millimeter-wave TWT.

1. Introduction

Recently, there is an increasing interest in the investigation on high power miniature traveling-wave tubes (TWTs) for potential applications in wideband millimeter wave and even Terahertz devices, such as millimeter wave radar and electronic-warfare [1]-[4]. As the core part of power amplifier for an electromagnetic (EM) wave, the slow-wave structures (SWSs) critically determine the performance of TWTs [5]. When the operating frequency increases to the millimeter-wave range, the output power of a TWT based on conventional SWSs decreases significantly due to beam-current density limitations, thermal-mechanical stability and fabrication

issues [6]. For these reasons, the investigation of novel SWSs for miniaturization of high-power millimeter-wave TWTs is very important.

The natural good properties of helix make it employ widely in the TWT for its flat dispersion characteristics and high interaction impedance. However, due to the electron beam going normally through the inner space of helix, the dimension of the beam tunnel is thus limited and reduces sharply with frequency increase, which leads to a small beam current and consequently decreasing output power. As so far the helix TWT can only works below 60GHz, and the manufacture and assembly become more difficult with shorter working wavelength. For breaking through the normal beam tunnel limit, can we use an electron beam with larger radius outside the helix? If so, the helix may work at W band and higher frequency range.

Meanwhile, the dielectric-lined azimuthally periodic circular waveguide (DLAP-CW), which has several peculiar characteristics of the large beam apertures and the high precision of manufacturing, is regarded as potential SWS for high-power TWTs at millimeter-wave and THz frequencies [7]. On the other hand, its high phase velocity may restrict the further application in the compact TWT interaction circuits, which indicates that the TWT based on such a structure need relatively higher operating voltage for satisfying the synchronous conditions in the beam-wave interaction.

Based upon above considerations, a novel helix-loaded azimuthally periodic circular waveguide (HLAP-CW) is now proposed for potential applications in high power broad band TWTs working at W band and higher frequency. The novel structure consists of helixes that are arranged periodically about the axis of the conventional circular waveguide, as shown in Fig.1.It inherits the unique properties of the conventional helix structure by inherently wide bandwidth, low dispersion and relatively high interaction efficiency [8], and N-helixes may interact with one electron beam having larger current for high output power ;furthermore, the microelectro-mechanical systems (MEMS) technologies [9]-[10] will alleviate the machining difficulties, which is helpful for a miniaturized radiation sources in millimeter and submillimeter-wave regimes [11]-[12]. Therefore, the HLAP-CW may be enabling SWS for miniaturized broad band high power millimeter-wave TWTs.

In this paper, the slow-wave characteristics of the HLAP-CW are studied by using the spatial harmonics method (SHM) [13] and the field-matching method with an appropriate eigenfunction expansion. The analysis has the advantages of very fast convergence and high accuracy [14]. In Section II, the field expressions, analytic dispersion and interaction impedance are obtained by SHM. The key challenge for the analysis of the HLAP-CW is how to satisfy the boundary conditions between the helixes, and then expand the solution based on the azimuthal periodicity. In Section III, the numerical results from Section II, including normalized phase velocity and interaction impedance, are compared with HFSS [15] simulations. Additionally, the relationships between the HLAP-CW slow-wave characteristics and the structure parameters are derived. A brief summary and conclusions are given in Section IV.

2. Theory

The configuration of the HLAP-CW is shown in Fig. 1, and can be analyzed in terms of the cylindrical coordinate system (r, φ, z). In this paper, the sidewise connection of the two-layer helical sheaths are ignored in order to investigate the RF properties of the novel structure conviently[16]. And helix made up of infinitely thin tape/wire. Regarding the structure geometry, L is the pitch, N is the number of helixes, the thickness of the helix cross section is represented by d and the angle of wedge $\varphi_{L,i}$ is equal to $\varphi_{e,i}$-$\varphi_{s,i}$. The structure has 1/N azimuthal symmetry, in other words, the angular period φ_p is $2\pi/N$.

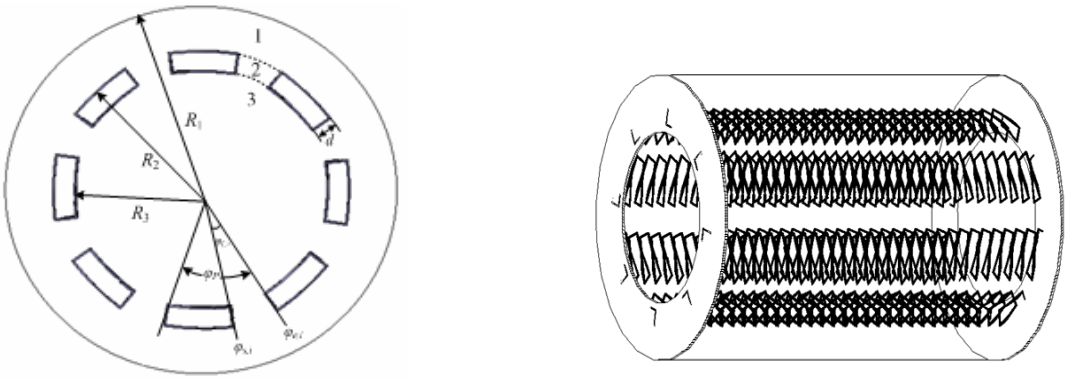

(a) (b)

Figure 1: Schematic of HLAP-CW. (a) cross-section of HLAP-CW (b) 3-D view of HLAP-CW

2.1 Field Expression and Boundary Conditions

Because of the azimuthal periodicity, Floquet theory is employed to derive the field expressions. The transverse field components can be expressed as a series of longitudinal field components, which is represented as a summation of spatial Bloch components. In addition, all the solutions in the HLAP-CW are hybrid modes (both TE and TM modes are required). Omitting $e^{(j\omega t - j\beta z)}$, the field expressions for E_z and H_z are derived, and the other field expressions can then be derived from them. In the subsequent analysis, ω represents the angular RF frequency, β represents the propagation constant, and m is the azimuthal mode index, which represents the periodicity of the RF field in the azimuthal direction. We divide the structure from Fig. 1 into four regions: Region 1 ($R_2<r<R_1$), Region 2 ($R_3<r<R_2$), Region 3 ($R_4<r<R_3$), and Region 4 ($r<R_4$).
In Region 1 ($R_2 < r < R_1$),

$$
\begin{aligned}
E_{1z} &= \sum_{n=-\infty}^{+\infty}[A_{1n}I_{k_n^{\mathrm{I}}}(k_{c1}r)+B_{1n}K_{k_n^{\mathrm{I}}}(k_{c1}r)]\exp(jk_n^{\mathrm{I}}\varphi)\\
H_{1z} &= \sum_{n=-\infty}^{+\infty}[C_{1n}I_{k_n^{\mathrm{I}}}(k_{c1}r)+D_{1n}K_{k_n^{\mathrm{I}}}(k_{c1}r)]\exp(jk_n^{\mathrm{I}}\varphi)\\
E_t &= \frac{1}{\beta^2-k_i^2}[j\omega\mu\vec{i}_z\times\nabla_t\vec{H}_z-j\beta\nabla_t\vec{E}_z]\\
H_t &= \frac{1}{\beta^2-k_i^2}[-j\omega\varepsilon\vec{i}_z\times\nabla_t\vec{E}_z-j\beta\nabla_t\vec{H}_z]
\end{aligned}
\tag{1}
$$

In Region 2 ($R_3 < r < R_2$), because helixes are arranged periodically about the axis of the circle waveguide, the field equations are expressed as an infinite sum of the eigen standing waves using Fourier expansion:

$$
\begin{aligned}
E_{2z,i} &= \sum_{l=1}^{+\infty}[A_{l,i}I_{k_{l,i}}(k_{c2}r)+B_{l,i}K_{k_{l,i}}(k_{c2}r)]\sin[k_{l,i}(\varphi-\varphi_{s,i})]\\
H_{2z,i} &= \sum_{l=1}^{+\infty}[C_{l,i}I_{k_{l,i}}(k_{c2}r)+D_{l,i}K_{k_{l,i}}(k_{c2}r)]\cos[k_{l,i}(\varphi-\varphi_{s,i})]
\end{aligned}
\tag{2}
$$

In Region 3 ($r < R_3$),

$$E_{3z} = \sum_{n=-\infty}^{+\infty} A_{3n} I_{k_n^{\mathrm{III}}}(k_{c3} r) \exp(j k_n^{\mathrm{III}} \varphi)$$
$$H_{3z} = \sum_{n=-\infty}^{+\infty} B_{3n} I_{k_n^{\mathrm{III}}}(k_{c3} r) \exp(j k_n^{\mathrm{III}} \varphi) \tag{3}$$

In (1)-(4), $k_{c1}^2 = k_{c2}^2 = k_{c3}^2 = \beta^2 - k_0^2$ are the transverse wavenumbers of Region 1, Region 2 and Region 3, respectively; $k_0^2 = \omega^2 \varepsilon_0 \mu_0$ is the wavenumber in free space with dielectric constant ε_0 and magnetic permeability μ_0. $k_n^I = k_n^{III} = nN + m$, and $k_{l,i} = l\pi/\varphi_{L,\mathrm{i}}$ are the azimuthal wavenumbers of Region 1, Region 3 and Region 2, respectively; and $A_{1\mathrm{n}}$, $B_{1\mathrm{n}}$, $C_{1\mathrm{n}}$, $D_{1\mathrm{n}}$, $A_{l,\mathrm{i}}$, $B_{l,\mathrm{i}}$, $C_{l,\mathrm{i}}$, $D_{l,\mathrm{i}}$, $A_{3\mathrm{n}}$ and $B_{3\mathrm{n}}$ are the amplitude coefficients of each region.

We now derive the boundary conditions at the interface between each region.

The tangential components of the electric field are continuous at $r=R_2$ and $r=R_3$, respectively, therefore

$$\sum_{i=1}^{N} \int_{\varphi_{s,i}}^{\varphi_{s,i+1}} E_{2z,i}\,|_{r=R_2}\, d\varphi = \int_0^{2\pi} E_{1z}\,|_{r=R_2}\, d\varphi \tag{4}$$

$$\sum_{i=1}^{N} \int_{\varphi_{s,i}}^{\varphi_{s,i+1}} E_{2z,i}\,|_{r=R_3}\, d\varphi = \int_0^{2\pi} E_{3z}\,|_{r=R_3}\, d\varphi \tag{5}$$

The electric field components along the helix direction are zero.

$$\int_{\varphi_{e,i}}^{\varphi_{s,i+1}} (E_{1z}\sin\psi + E_{1\varphi}\cos\psi)\,|_{r=R_2}\, d\varphi = 0 \tag{6}$$

$$\int_{\varphi_{e,i}}^{\varphi_{s,i+1}} (E_{3z}\sin\psi + E_{3\varphi}\cos\psi)\,|_{r=R_3}\, d\varphi = 0 \tag{7}$$

Finally, the tangential component of the electric field is zero at the boundary of the perfect electric conductor at R_1:

$$E_{1z}\big|_{r=R_1} = 0 \tag{8}$$

$$E_{1\varphi}\big|_{r=R_1} = 0 \tag{9}$$

2.2 Dispersion Equation

Substituting the field expressions from each region into the aforementioned boundary conditions to eliminate the amplitude constants, the corresponding frequency for every given axial wavenumber β is then determined, *i.e.*, the dispersion relation is found from the following expression:

$$Det\begin{bmatrix} A_{1n}^{(1)} & B_{1n}^{(1)} & 0 & 0 & 0 & 0 \\ A_{1n}^{(2)} & B_{1n}^{(2)} & C_{1n}^{(2)} & D_{1n}^{(2)} & 0 & 0 \\ A_{1n}^{(3)} & B_{1n}^{(3)} & C_{1n}^{(3)} & D_{1n}^{(3)} & 0 & 0 \\ A_{1nq}^{(4)} & B_{1nq}^{(4)} & 0 & 0 & 0 & 0 \\ 0 & 0 & 0 & 0 & A_{3n}^{(5)} & B_{3n}^{(5)} \\ 0 & 0 & 0 & 0 & A_{3nq}^{(6)} & 0 \end{bmatrix} = 0 \tag{10}$$

Where,

$$A_{1n}^{(1)} = I_{k_n^{\mathrm{I}}}(k_{c1}R_1), \quad B_{1n}^{(1)} = K_{k_n^{\mathrm{I}}}(k_{c1}R_1),$$

$$A_{1n}^{(2)} = \frac{-j\beta k_n^{\mathrm{I}}}{k_{c1}^2 R_1} I_{k_n^{\mathrm{I}}}(k_{c1}R_1) \quad B_{1n}^{(2)} = \frac{-j\beta k_n^{\mathrm{I}}}{k_{c1}^2 R_1} K_{k_n^{\mathrm{I}}}(k_{c1}R_1),$$

$$C_{1n}^{(2)} = \frac{j\omega\mu\sin\phi}{k_{c1}} I'_{k_n^{\mathrm{I}}}(k_{c1}R_1), \quad D_{1n}^{(2)} = \frac{j\omega\mu\sin\phi}{k_{c1}} K'_{k_n^{\mathrm{I}}}(k_{c1}R_1),$$

$$A_{1n}^{(3)} = I_{k_n^{\mathrm{I}}}(k_{c1}R_2)(\sin\psi - \frac{j\beta k_n^{\mathrm{I}}}{k_{c1}^2 R_2}\cos\psi)(\varphi_{s,i+1} - \varphi_{e,i})$$

$$B_{1n}^{(3)} = K_{k_n^{\mathrm{I}}}(k_{c1}R_2)(\sin\psi - \frac{j\beta k_n^{\mathrm{I}}}{k_{c1}^2 R_2}\cos\psi)(\varphi_{s,i+1} - \varphi_{e,i}), \quad C_{1n}^{(3)} = \frac{j\omega\mu\cos\psi}{k_{c1}} I'_{k_n^{\mathrm{I}}}(k_{c1}R_2)(\varphi_{s,i+1} - \varphi_{e,i}),$$

$$D_{1n}^{(3)} = \frac{j\omega\mu\cos\psi}{k_{c1}} I'_{k_n^{\mathrm{I}}}(k_{c1}R_2)(\varphi_{s,i+1} - \varphi_{e,i}),$$

$$A_{1nq}^{(4)} = \sum_{l=1}^{+\infty}\sum_{i=1}^{N}\sum_{q=-\infty}^{+\infty}[I_{k_q^{\mathrm{I}}}(k_{c1}R_2)R(k_q^{\mathrm{I}}, k_{l,i})R(-k_n^{\mathrm{I}}, k_{l,i})\frac{4}{2\varphi_p - \sin(2k_{l,i}\varphi_p)}] - 2\pi\delta_{nq}I_{k_n^{\mathrm{I}}}(k_{c1}R_2)$$

$$B_{1nq}^{(4)} = \sum_{l=1}^{+\infty}\sum_{i=1}^{N}\sum_{q=-\infty}^{+\infty}[K_{k_q^{\mathrm{I}}}(k_{c1}R_2)R(k_q^{\mathrm{I}}, k_{l,i})R(-k_n^{\mathrm{I}}, k_{l,i})\frac{4}{2\varphi_p - \sin(2k_{l,i}\varphi_p)}] - 2\pi\delta_{nq}K_{k_n^{\mathrm{I}}}(k_{c1}R_2)$$

$$A_{3n}^{(5)} = I_{k_n^{\mathrm{III}}}(k_{c1}R_3)(\sin\psi - \frac{j\beta k_n^{\mathrm{III}}}{k_{c1}^2 R_3}\cos\psi)(\varphi_{s,i+1} - \varphi_{e,i}) \quad B_{3n}^{(5)} = \frac{j\omega\mu\cos\psi}{k_{c1}} I'_{k_n^{\mathrm{III}}}(k_{c1}R_3)(\varphi_{s,i+1} - \varphi_{e,i})$$

$$A_{3nq}^{(6)} = \sum_{l=1}^{+\infty}\sum_{i=1}^{N}\sum_{q=-\infty}^{+\infty}[I_{k_q^{\mathrm{III}}}(k_{c1}R_3)R(k_q^{\mathrm{III}}, k_{l,i})R(-k_n^{\mathrm{III}}, k_{l,i})\frac{4}{2\varphi_p - \sin(2k_{l,i}\varphi_p)}] - 2\pi\delta_{nq}I_{k_n^{\mathrm{III}}}(k_{c1}R_3)$$

In the practical calculation, a sufficiently accurate result with the relative error less than 10^{-6} can be got by considering only three terms (n=-1, 0, 1).

$$
\begin{vmatrix}
A_{1,-1}^{(1)} & B_{1,-1}^{(1)} & 0 & 0 & 0 & 0 & 0 & 0 & 0 & 0 & 0 & 0 & 0 & 0 & 0 & 0 & 0 & 0 \\
0 & 0 & 0 & 0 & 0 & 0 & A_{1,0}^{(1)} & B_{1,0}^{(1)} & 0 & 0 & 0 & 0 & 0 & 0 & 0 & 0 & 0 & 0 \\
0 & 0 & 0 & 0 & 0 & 0 & 0 & 0 & 0 & 0 & 0 & 0 & A_{1,1}^{(1)} & B_{1,1}^{(1)} & 0 & 0 & 0 & 0 \\
A_{1,-1}^{(2)} & B_{1,-1}^{(2)} & C_{1,-1}^{(2)} & D_{1,-1}^{(2)} & 0 & 0 & 0 & 0 & 0 & 0 & 0 & 0 & 0 & 0 & 0 & 0 & 0 & 0 \\
0 & 0 & 0 & 0 & 0 & 0 & A_{1,0}^{(2)} & B_{1,0}^{(2)} & C_{1,0}^{(2)} & D_{1,0}^{(2)} & 0 & 0 & 0 & 0 & 0 & 0 & 0 & 0 \\
0 & 0 & 0 & 0 & 0 & 0 & 0 & 0 & 0 & 0 & 0 & 0 & A_{1,1}^{(2)} & B_{1,1}^{(2)} & C_{1,1}^{(2)} & D_{1,1}^{(2)} & 0 & 0 \\
A_{1,-1}^{(3)} & B_{1,-1}^{(3)} & C_{1,-1}^{(3)} & D_{1,-1}^{(3)} & 0 & 0 & 0 & 0 & 0 & 0 & 0 & 0 & 0 & 0 & 0 & 0 & 0 & 0 \\
0 & 0 & 0 & 0 & 0 & 0 & A_{1,0}^{(3)} & B_{1,0}^{(3)} & C_{1,0}^{(3)} & D_{1,0}^{(3)} & 0 & 0 & 0 & 0 & 0 & 0 & 0 & 0 \\
0 & 0 & 0 & 0 & 0 & 0 & 0 & 0 & 0 & 0 & 0 & 0 & A_{1,1}^{(3)} & B_{1,1}^{(3)} & C_{1,1}^{(3)} & D_{1,1}^{(3)} & 0 & 0 \\
A_{1,-1,-1}^{(4)} & B_{1,-1,-1}^{(4)} & 0 & 0 & 0 & 0 & A_{1,-1,0}^{(4)} & B_{1,-1,0}^{(4)} & 0 & 0 & 0 & 0 & A_{1,-1,1}^{(4)} & B_{1,-1,1}^{(4)} & 0 & 0 & 0 & 0 \\
A_{1,0,-1}^{(4)} & B_{1,0,-1}^{(4)} & 0 & 0 & 0 & 0 & A_{1,0,0}^{(4)} & B_{1,0,0}^{(4)} & 0 & 0 & 0 & 0 & A_{1,0,1}^{(4)} & B_{1,0,1}^{(4)} & 0 & 0 & 0 & 0 \\
A_{1,1,-1}^{(4)} & B_{1,1,-1}^{(4)} & 0 & 0 & 0 & 0 & A_{1,1,0}^{(4)} & B_{1,1,0}^{(4)} & 0 & 0 & 0 & 0 & A_{1,1,1}^{(4)} & B_{1,1,1}^{(4)} & 0 & 0 & 0 & 0 \\
0 & 0 & 0 & 0 & A_{3,-1}^{(5)} & B_{3,-1}^{(5)} & 0 & 0 & 0 & 0 & 0 & 0 & 0 & 0 & 0 & 0 & 0 & 0 \\
0 & 0 & 0 & 0 & 0 & 0 & 0 & 0 & 0 & 0 & A_{3,0}^{(5)} & B_{3,0}^{(5)} & 0 & 0 & 0 & 0 & 0 & 0 \\
0 & 0 & 0 & 0 & 0 & 0 & 0 & 0 & 0 & 0 & 0 & 0 & 0 & 0 & 0 & 0 & A_{3,1}^{(5)} & B_{3,1}^{(5)} \\
0 & 0 & 0 & 0 & A_{3,-1,-1}^{(6)} & 0 & 0 & 0 & 0 & 0 & A_{3,-1,0}^{(6)} & 0 & 0 & 0 & 0 & 0 & A_{3,-1,1}^{(6)} & 0 \\
0 & 0 & 0 & 0 & A_{3,0,-1}^{(6)} & 0 & 0 & 0 & 0 & 0 & A_{3,0,0}^{(6)} & 0 & 0 & 0 & 0 & 0 & A_{3,0,1}^{(6)} & 0 \\
0 & 0 & 0 & 0 & A_{3,1,-1}^{(6)} & 0 & 0 & 0 & 0 & 0 & A_{3,1,0}^{(6)} & 0 & 0 & 0 & 0 & 0 & A_{3,1,1}^{(6)} & 0
\end{vmatrix} = 0
$$

2.3 Interaction Impedance

The interaction impedance in linear-beam microwave tubes represents the strength of the beam-wave interaction, and it is defined as

$$K_c = \frac{E_{zn} \cdot E_{zn}^*}{2\beta_n^2 P} = \frac{[A_{3n} I_{k_n^{\mathrm{III}}}(k_{c1} R_{beam})]^2}{2\beta_n^2 (\sum_{n=-\infty}^{+\infty} P_1 + \sum_{l=1}^{+\infty} P_2 + \sum_{n=-\infty}^{+\infty} P_3)} \tag{11}$$

where E_{zn} is the on-axis electric field of the nth space harmonic, E_{zn}^* is its conjugate, β_n is the axial wavenumber of the nth space harmonic, and P is the total power flow in the z- direction (axial power flow). In (11), P can be expressed as

$$P = \frac{1}{2} \mathrm{Re} \iint_S (E_r H_\varphi^* - E_\varphi H_r^*) r dr d\varphi \tag{12}$$

Therefore, the axial power flows through each region is obtained as

$$
\begin{aligned}
P_1 &= \frac{1}{2}\mathrm{Re}\int_{R_0}^{R_1}\int_0^{2\pi}\{-\frac{j\beta}{k_{c1}}[A_{1n}I_{k_n^{\mathrm{I}}}(k_{c1}r)+B_{1n}K_{k_n^{\mathrm{I}}}(k_{c1}r)]-\frac{j\omega\mu k_n^{\mathrm{I}}}{k_{c1}^2}\frac{1}{r}[C_{1n}I_{k_n^{\mathrm{I}}}(k_{c1}r)+D_{1n}K_{k_n^{\mathrm{I}}}(k_{c1}r)]\}\{\frac{j\omega\varepsilon}{k_{c1}}[A_{1n}I_{k_n^{\mathrm{I}}}(k_{c1}r)+B_{1n}K_{k_n^{\mathrm{I}}}(k_{c1}r)]+\frac{j\beta k_n^{\mathrm{I}}}{k_{c1}^2}\frac{1}{r}[C_{1n}I_{k_n^{\mathrm{I}}}(k_{c1}r)+D_{1n}K_{k_n^{\mathrm{I}}}(k_{c1}r)]\}rdrd\varphi \\
&\quad -\frac{1}{2}\mathrm{Re}\int_{R_0}^{R_1}\int_0^{2\pi}\{-\frac{j\beta k_n^{\mathrm{I}}}{k_{c1}^2}\frac{1}{r}[A_{1n}I_{k_n^{\mathrm{I}}}(k_{c1}r)+B_{1n}K_{k_n^{\mathrm{I}}}(k_{c1}r)]+\frac{j\omega\mu}{k_{c1}}[C_{1n}I_{k_n^{\mathrm{I}}}(k_{c1}r)+D_{1n}K_{k_n^{\mathrm{I}}}(k_{c1}r)]\}\{-\frac{j\omega\varepsilon k_n^{\mathrm{I}}}{k_{c1}^2}\frac{1}{r}[A_{1n}I_{k_n^{\mathrm{I}}}(k_{c1}r)+B_{1n}K_{k_n^{\mathrm{I}}}(k_{c1}r)]+\frac{j\beta}{k_{c1}}[C_{1n}I_{k_n^{\mathrm{I}}}(k_{c1}r)+D_{1n}K_{k_n^{\mathrm{I}}}(k_{c1}r)]\}rdrd\varphi \\
P_2 &= \mathrm{Re}\{\sum_{i=1}^{N}\int_{R_3}^{R_2}\int_{\varphi_{s,i}}^{\varphi_{s,i}+\theta_i} F_1F_2\sin^2[k_{z,i}(\varphi-\varphi_{s,i})]rdrd\varphi - \sum_{i=1}^{N}\int_{R_3}^{R_2}\int_{\varphi_{s,i}}^{\varphi_{s,i}+\theta_i} F_3F_4\cos^2[k_{z,i}(\varphi-\varphi_{s,i})]rdrd\varphi\} \\
P_3 &= \frac{1}{2}\mathrm{Re}\int_0^{R_3}\int_0^{2\pi}[-\frac{j\beta}{k_{c1}}A_{3n}I'_{k_n^{\mathrm{III}}}(k_{c1}r)-\frac{j\omega\mu k_n^{\mathrm{III}}}{k_{c1}^2}\frac{1}{r}B_{3n}I_{k_n^{\mathrm{I}}}(k_{c1}r)][\frac{j\omega\varepsilon}{k_{c1}}A_{3n}I'_{k_n^{\mathrm{III}}}(k_{c1}r)+\frac{j\beta}{k_{c1}^2}\frac{k_n^{\mathrm{III}}}{r}B_{3n}I_{k_n^{\mathrm{III}}}(k_{c1}r)]rdrd\varphi \\
&\quad -\frac{1}{2}\mathrm{Re}\int_0^{R_3}\int_0^{2\pi}[-\frac{j\beta}{k_{c1}^2}\frac{k_n^{\mathrm{III}}}{r}A_{3n}I_{k_n^{\mathrm{III}}}(k_{c1}r)+\frac{j\omega\mu}{k_{c1}}B_{1n}I'_{k_n^{\mathrm{III}}}(k_{c1}r)][-\frac{j\omega\varepsilon}{k_{c1}^2}\frac{k_n^{\mathrm{III}}}{r}A_{3n}I_{k_n^{\mathrm{III}}}(k_{c1}r)+\frac{j\beta}{k_{c1}}B_{3n}I'_{k_n^{\mathrm{III}}}(k_{c1}r)]rdrd\varphi
\end{aligned} \tag{13}
$$

Where,

$$F_1 = -\frac{j\beta}{k_{c1}}[A_{l,i}I'_{k_{l,i}}(k_{c2}r) + B_{l,i}K'_{k_{l,i}}(k_{c2}r)] + \frac{j\omega\mu k_{l,i}}{k_{c1}^2}[C_{l,i}I_{k_{l,i}}(k_{c1}r) + D_{l,i}K_{k_{l,i}}(k_{c1}r)]$$

$$F_2 = \frac{j\omega\varepsilon}{k_{c1}}[A_{l,i}I'_{k_{l,i}}(k_{c2}r) + B_{l,i}K'_{k_{l,i}}(k_{c2}r)] - \frac{j\beta}{k_{c1}^2}\frac{k_{l,i}}{r}[C_{l,i}I_{k_{l,i}}(k_{c1}r) + D_{l,i}K_{k_{l,i}}(k_{c1}r)]$$

$$F_3 = -\frac{j\beta}{k_{c1}^2}\frac{k_{l,i}}{r}[A_{l,i}I_{k_{l,i}}(k_{c1}r) + B_{l,i}K_{k_{l,i}}(k_{c1}r)] + \frac{j\omega\mu}{k_{c1}}[C_{l,i}I'_{k_{l,i}}(k_{c2}r) + D_{l,i}K'_{k_{l,i}}(k_{c2}r)]$$

$$F_4 = \frac{-j\omega\varepsilon}{k_{c1}^2}\frac{k_{l,i}}{r}[A_{l,i}I_{k_{l,i}}(k_{c1}r) + B_{l,i}K_{k_{l,i}}(k_{c1}r)] + \frac{j\beta}{k_{c1}}[C_{l,i}I'_{k_{l,i}}(k_{c2}r) + D_{l,i}K'_{k_{l,i}}(k_{c2}r)] \quad (14)$$

The relative values of A_{1n}, B_{1n}, C_{1n}, D_{1n}, $A_{l,i}$, $B_{l,i}$, $C_{l,i}$, $D_{l,i}$, A_{3n} and B_{3n} can be reduced by solving the (1)-(3) with an orthgonality relation. Then, the interaction impedance of the HLAP-CW is obtained.

3. Numerical Results and Discussions

The dispersion equation (10) and the interaction impedance equation (14) can be solved numerically using the Matlab computer software package [17]. Here, we present the numerical results for the slow-wave characteristics of the helix-loaded azimuthally periodic circular waveguide.

In order to verify the correctness of the present theory, the Matlab results are compared with those simulated using HFSS [15]. In our simulation, the total number of mesh refinement is more than two ten thousand for the structure with the discretisation error of 0.021216 in center operation frequency. This comparison is shown in Fig. 2. The figure shows the dispersion characteristics and the interaction impedance of for an HLAP-CW with R_2/R_1=0.75, d/R_1=0.1, L/R_1=0.2, $\varphi_{L,i}/\varphi_p$=0.4, N=8 and R_1=1 mm. It is clear that the numerical results from the present theory agree well with the results from HFSS.

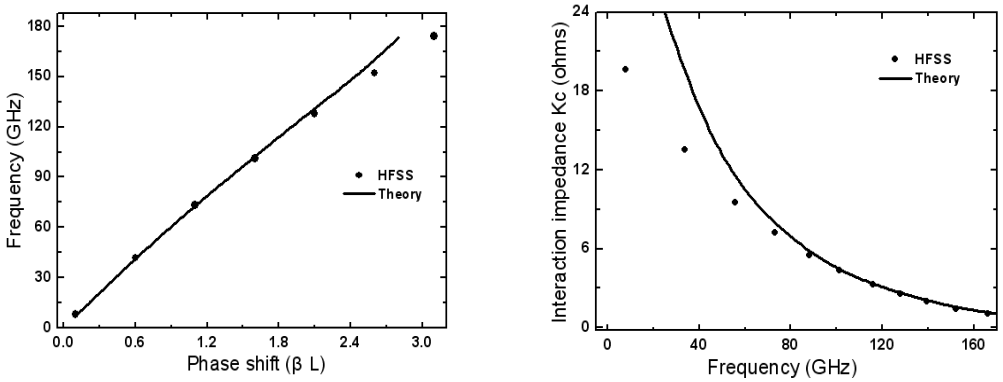

Figure 2: (a) Dispersion curve of HLAP-CW and (b) Interaction impedance of HLAP-CW calculated using the present theory and HFSS

We now investigate the effects of the structure parameters on the slow-wave properties of the HLAP-CW based on the present theory. Figure 3 shows the effect of the pitch on the normalized phase velocity and the interaction impedance of the HLAP-CW. Here, the structure parameters are the same as those in Fig. 2. It can be seen that the normalized phase velocity increases as the pitch increases. This effect is mainly caused by the fact that increasing the pitch of the helix makes the actual propagation distance of the electromagnetic wave become shorter in the case of the same axial distance. Further researches indicate that the variation trend of the interaction impedance with

the pitch variation is non-linear relationship, as shown in Fig. 2(b). When the pitch increases, the interaction impedance decreases in the low frequency of the operating band, and then increases in the high frequency. In addition, the operating bandwidth is also reduced with the increase of the pitch. It is therefore necessary to choose the proper pitch parameter for meeting desired device bandwidth and interaction impedance.

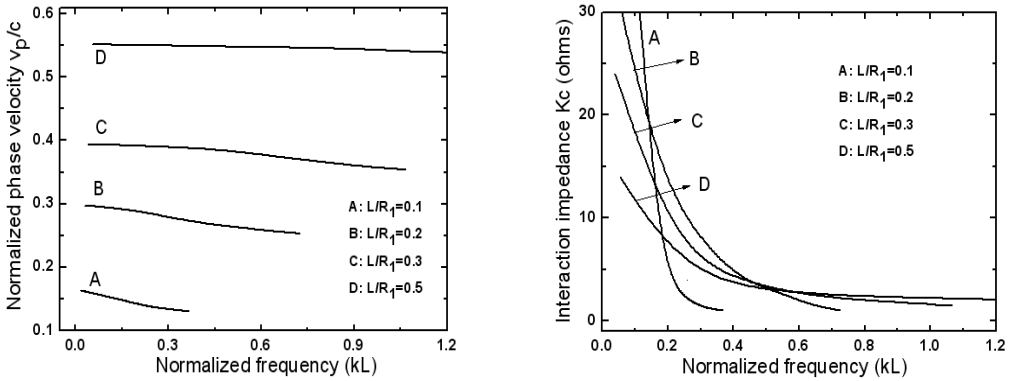

(a) normalized phase velocity and (b) interaction impedance.

Figure 3: Comparison of the slow-wave characteristics for HLAP-CW with R_2/R_1=0.75, d/R_1=0.1, $\varphi_{L,i}/\varphi_p$=0.4, N=8 and R_1=1 mm:

The effect of the dielectric constant of the structure on the slow-wave characteristics of the HLAP-CW is studied in Fig. 4, where the pitch of the helix held fixed at 0.1. The results are shown that the normalized phase velocity, the operating bandwidth and the interaction impedance all decreases when the dielectric constant increases. And the dispersion curve becomes more flatter at the same time.

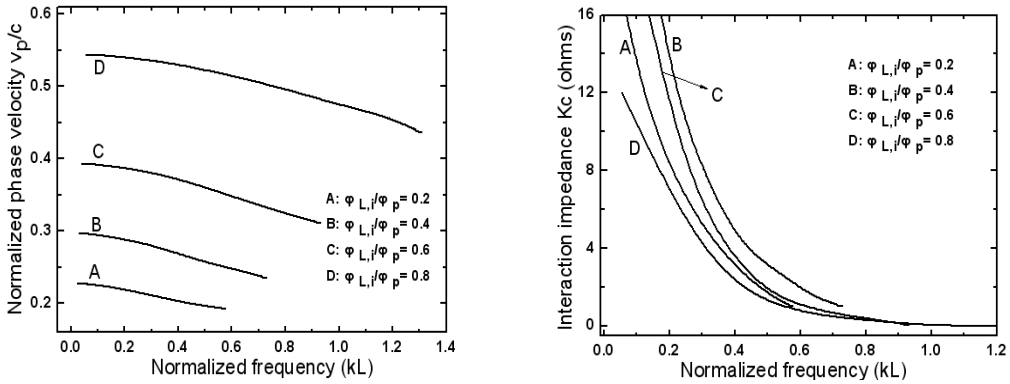

(a) normalized phase velocity and (b) interaction impedance.

Figure 4: Comparison of the slow-wave characteristics for DLAP-CW with R_2/R_1=0.75, d/R_1=0.1, L/R_1=0.2, N=8 and R_1=1 mm:

In Fig. 5, the normalized phase velocity and the interaction impedance for several widths of the helix cross section are plotted versus frequency while the pitch and the angle are fixed. It is clear that the phase velocity decreases, and the dispersion curve flattens when the width becomes wider, which indicates that the synchronous beam voltage can be reduced by decreasing the width of the helix cross section. At the same time, the interaction impedance initially increases but then decreases, which has a similar trend to that in Fig. 4(b). Curve C in Fig. 5(b) indicates that the interaction impedance of the HLAP-CW with d/R_1 = 0.1 is optimal. The angle and the width of the helix cross section for a specific HLAP-CW design must be carefully optimized to improve the performance of the beam-wave interaction in an HLAP-CW-based TWT.

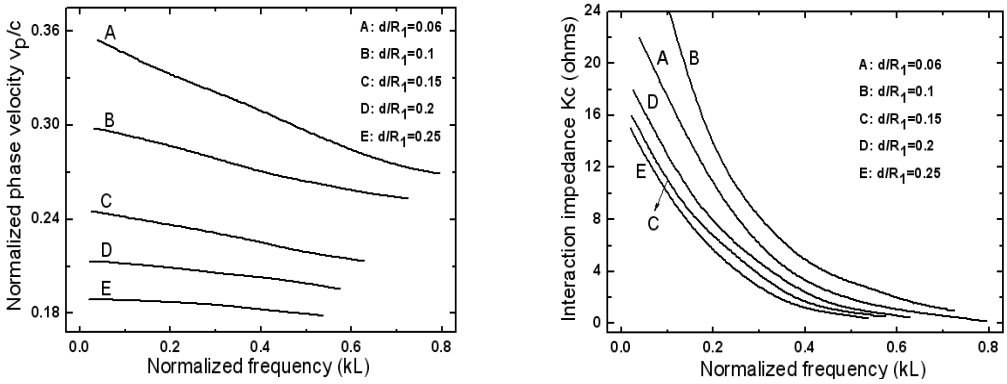

(a) normalized phase velocity and (b) interaction impedance.

Figure 5: Comparison of the slow-wave characteristics for DLAP-CW with R_2/R_1=0.75, L/R_1=0.2, $\varphi_{L,i}/\varphi_p$=0.4, N=8 and R_1=1 mm:

Finally, we compare the performances of the HLAP-CW and the DLAP-CW in the case of the same structure parameters, where the structure parameters are the same as those in Fig. 2. In Fig. 6, the results show that the operating bandwidth of the HLAP-CW is much wider than that of the DLAP-CW, and the normalized phase velocity of the HLAP-CW is also much lower. It is proved that the HLAP-CW can effectively reduce the interaction voltage. Furthermore, Fig. 6 (b) reveals that the interaction impedance of the HLAP-CW is much higher than that of the DLAP-CW in the operating band. The higher interaction impedance indicates that the HLAP-CW can effectively improve the interaction efficiency, which may lead to a higher gain. In other words, the HLAP-CW may reach a higher gain with the same tube length or obtain the same gain with a smaller tube length since the gain of a tube increases as the averaged coupling impedance increases. Therefore, the HLAP-CW is more suitable for application in compact TWTs than that of the DLAP-CW.

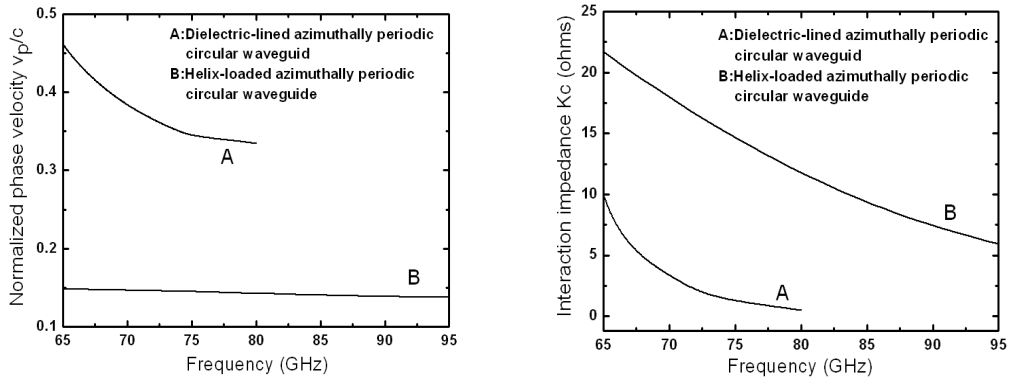

Figure 6: Comparison of the slow-wave characteristics for DLAP-CW with ε=20, R_2/R_1=0.75, d/R_1=0.1, R_4/R_1=0.3, $\varphi_{L,i}/\varphi_p$=0.4, N=8 and R_1=1 mm and R_4=2 mm and DLAP-CW with R_2/R_1=0.75, d/R_1=0.1, L/R_1=0.1, $\varphi_{L,i}/\varphi_p$=0.4, N=8 and R_1=1 mm: (a) normalized phase velocity and (b) interaction impedance.

4. Conclusion

In this paper a novel linear-beam TWT circuit structure, the helix-loaded azimuthally periodic circular waveguide (HLAP-CW), has been investigated. Equations for the slow-wave characteristics including phase velocity and interaction impedance are derived using the spatial harmonics method, and the solutions are validated by HFSS. The numerical results reveal that the influence of the pitch, the angle and the width of the helix cross section all significantly impact the HLAP-CW slow-wave characteristics. Furthermore, compared with a dielectric-lined azimuthally periodic circular

waveguide (DLAP-CW), the interaction impedance of the HLAP-CW is much higher than that of the DLAP-CW across the operating band, which implies that there will be a significant improvement in the interaction efficiency of a HLAP-CW-based TWT. On the other hand, the operating bandwidth of the HLAP-CW is also much wider with the lower phase velocity. The lower phase velocity proves that the HLAP-CW can effectively reduce the interaction voltage, so the DLAP-CW holds promise for compact TWT application. Therefore, the novel HLAP-CW structure has potential for application in compact broad band millimeter wave and even Terahertz devices.

Acknowledgements

This work was supported by Science and Technology Plan Project of Sichuan (Key project) under Grant No.2022YFG0195.

References

[1] C. Kory, L. Ives, J. Booske, S. Bhattacharjee et al., "Novel TWT interaction circuits for high frequency applications," in Proc. 5th IEEE Int. Vacuum Electron. Conf., Eur. Space Agency, Apr. 2004, pp. 51–52.
[2] C. K. Chong, J. A. Davis, R. H. Le Brogne et al., "Development of high-power Ka-band and Q-band helix-TWTs ," IEEE Trans. Electron Devices, vol. 52, no. 2, pp. 653-659, May 2005.
[3] W. L. Menninger, N. R. Robbins, D. E. Dibb et al., "Power flexible Ka-band traveling wave tube amplifiers of up to 250-W RF for space communications," IEEE Trans. Electron Devices, vol. 54, pp. 181-187, Feb. 2007.
[4] C. R.Donaldson, Wenlong He, Adrian W. Cross et al., "Design and numerical optimization of a cusp-gun-based electron beam for millimeter-wave gyro-devices," IEEE Trans. Plasma Science, vol. 37, pp. 2153-2157,Mov. 2009.
[5] W. Wang, Y. Wei, G. Yu, Y. Gong, M. Huang, and G. Zhao, "Review of the novel slow-wave structures for high-power traveling-wave tube," Int. J. Infrared Millim. Waves, vol. 24, no. 9, pp. 1469–1484, Sep. 2003.
[6] Y. B. Gong, Y.Y. Wei, M.Z. Huang et al., "Research activities on millimeter wave TWT in UESTC," in GMSS, China, 2008, pp. 978-981.
[7] Yang Liu, Y.Y. Wei, Y. B. Gong and W. W. Wang, "Investigation on the Slow-Wave Properties of a Dielectric-Lined Azimuthally Periodic Circular Waveguide for TWT," IEEE Trans. Electron Devices, vol. 57, pp. 2019-2026, Aug. 2010.
[8] Sun-Shin Jung, Chan-Wook Baik, Seong-Tae Han et al., "Wide-Band Semivane and Heavily Dielectric Loaded Helix Traveling-Wave Tubes," IEEE Trans. Plasma Science, vol. 30, pp. 1009-1016, Jun. 2002.
[9] James A. Dayton, Jr., Carol L. Kory, Gerald T. Mearini et al., "Applying Microfabrication to Helical Vacuum Electron Devices for THz Applications," in IEEE International Vacuum Electronics Conference, Apr. 2009, pp. 41–44.
[10] Carol L. Kory, James A. Dayton, Jr., Gerald T. Mearini et al., "95 GHz Helical TWT Design," in IEEE International Vacuum Electronics Conference, Apr. 2009, pp. 125–126.
[11] James A. Dayton, Jr., Carol L. Kory, Gerald T. Mearini et al., "A 650 GHz Helical BWO," in IEEE International Vacuum Electronics Conference, Apr. 2008, pp. 396–397.
[12] Carol L. Kory and James A. Dayton, Jr., "Design of 650 GHz Helical BWO Using CST Studio Suite," in IEEE International Vacuum Electronics Conference, Apr. 2008, pp. 392–393.
[13] R. E. Collin, Field Theory of Guided Waves, New York: McGraw-Hill, 1960, ch. 11.
[14] Z. C. Ioannidis, O. Dumbrajs, and I. G. Tigelis, "Eigenvalues and ohmic losses in coaxial gyrotron cavity," IEEE Trans. Plasma Sci., vol. 32, no. 3, pp. 861-866, Jun. 2004.
[15] "High frequency structure simulator user's reference," Anosft Corp., 2001. (more information available online: [http://www.ansoft.com/])
[16] R. K. Arora, "Surface wave on a pair of parallel unidirectionlly conducting screens," IEEE Trans.Antennas Propagat, AT-14, pp. 795-797,1966 .
[17] Getting Started. Matlab help v 7.0.1., the Mathworks. Inc., Natick, Massachusetts., 2004. (more information available online: [http://www.mathworks.com/])